RESEARCH ARTICLE

NANO · MICRO small
www.small-journal.com

Bio-Inspired Fluorescent Calcium Sulfate for the Conservation of Gypsum Plasterwork

Miguel Burgos-Ruiz, Martha Ilett, Teresa Roncal-Herrero, Kerstin Elert, Ramon Rubio-Domene, Encarnacion Ruiz-Agudo, and Carlos Rodriguez-Navarro*

In this work, the potential of bio-inspired strategies for the synthesis of calcium sulfate ($CaSO_4 \cdot nH_2O$) materials for heritage conservation is explored. For this, a nonclassical multi-step crystallization mechanism to understand the effect of calcein– a fluorescent chelating agent with a high affinity for divalent cations— on the nucleation and growth of calcium sulfate phases is proposed. Moving from the nano- to the macro-scale, this strategy sets the basis for the design and production of fluorescent nano-bassanite (NB-C; $CaSO_4 \cdot 0.5H_2O$), with application as a fully compatible consolidant for the conservation of historic plasterwork. Once applied to gypsum ($CaSO_4 \cdot 2H_2O$) plaster specimens, cementation upon hydration of nano-bassanite results in a significant increase in mechanical strength, while intracrystalline occlusion of calcein in newly-formed gypsum cement improves its weathering resistance. Furthermore, under UV irradiation, the luminescence produced by calcein molecules occluded in gypsum crystals formed upon nano-bassanite hydration allows the easy identification of the newly deposited consolidant within the treated gypsum plaster without altering the substrate's appearance.

1. Introduction

As an important branch of materials science and solid-state chemistry, crystal engineering stands out as a versatile discipline that offers innovative solutions for a multitude of modern-day problems through the design and manipulation of crystal structures to produce materials with tailored advanced functionalities, ranging, for example, from biomedical and drug-delivery applications to the development of highly efficient semi-conductors, as well as nanoelectronic and optical devices.[1–4] In this context, biomimicry has drawn the attention of the scientific community over the last 2 decades as a powerful tool, for example, for replicating the properties of materials produced by living organisms.[5,6]

While the synthesis of biomaterials presents significant challenges, researchers have made remarkable progress by employing bio-mimetic and bio-inspired strategies, including the use of organic monomeric and/or polymeric species to artificially reproduce the effect of proteins and polysaccharides involved in natural biomineralization processes.[7–11] An illustrative example of such progress is the work of Cölfen et al., who extensively investigated the impact of organic templates and additives on the crystallization of calcium carbonate ($CaCO_3$), among other phases.[12–15] They successfully developed mesoscale methodologies for the fabrication of complex biomimetic 3D superstructures, such as synthetic nacre and vaterite mesocrystals showing enhanced stability.[16,17] However, these strategies have not been investigated in the case of calcium sulfates ($CaSO_4 \cdot nH_2O$). Although they are not the most prevalent biominerals in nature, bassanite ($CaSO_4 \cdot 0.5H_2O$) has been described as the main mineral phase present in the statoliths of diverse Cubozoan and Scyphozoan medusae, serving as gravity and inertia sensors.[18–20] Gypsum ($CaSO_4 \cdot 2H_2O$) has been also found to be part of the impact surface in the raptorial appendages of some species of stomatopod crustaceans of the *Odontodactylus scyllarus* type (better known as "mantis shrimps"), which they use as powerful hammers propelled at extreme speeds of about 23 m s^{-1} to break mollusk shells.[21]

Furthermore, there is ample evidence proving that biomimetic approaches have been employed since ancient times for the elaboration of lime-based building and ornamental materials, whether fortuitously or intentionally, to elaborate durable

M. Burgos-Ruiz, K. Elert, E. Ruiz-Agudo, C. Rodriguez-Navarro
Department of Mineralogy and Petrology
Faculty of Sciences
University of Granada
Avenida Fuentenueva S/N, Granada 18002, Spain
E-mail: miguelburgos95@ugr.es
M. Ilett, T. Roncal-Herrero
School of Chemical and Process Engineering
University of Leeds
Woodhouse, Leeds LS2 9JT, UK
K. Elert
Escuela de Estudios Árabes
Spanish National Research Council (CSIC)
Cuesta del Chapiz 22, Granada 18010, Spain
R. Rubio-Domene
Conservation Department
Council of the Alhambra and Generalife
Calle Real de la Alhambra S/N, Granada E-18009, Spain

The ORCID identification number(s) for the author(s) of this article can be found under https://doi.org/10.1002/smll.202402581

DOI: 10.1002/smll.202402581

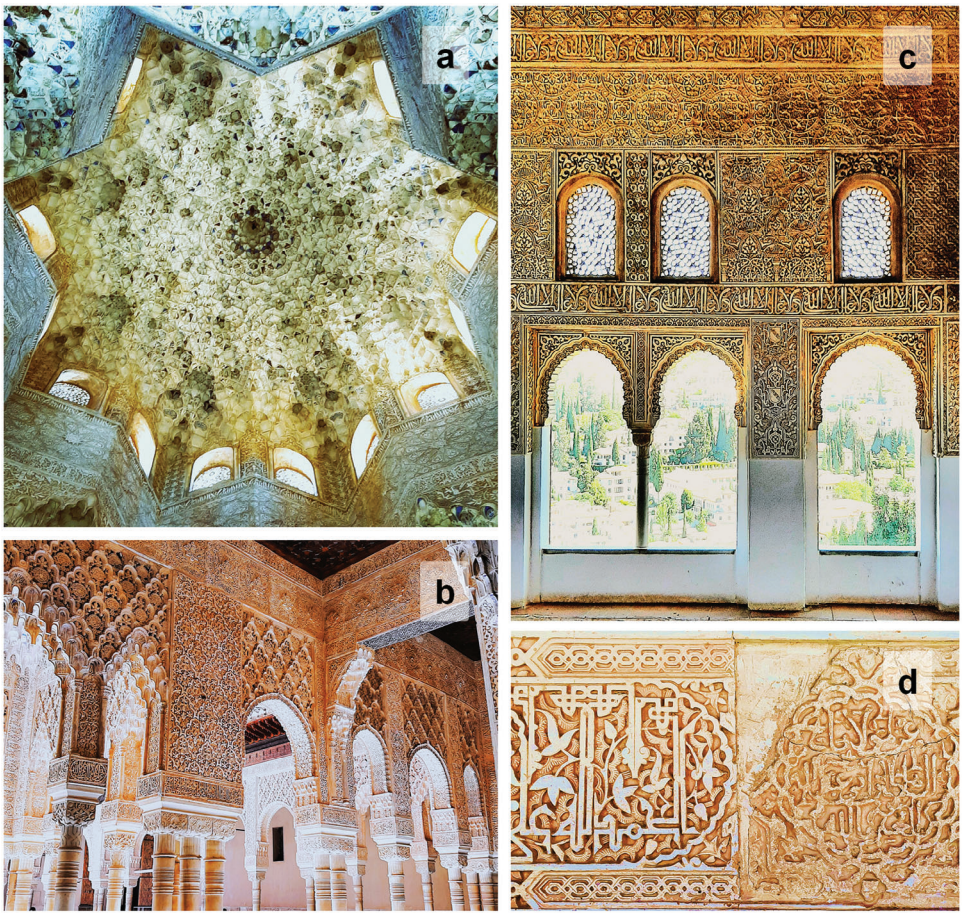

Figure 1. General view of muqarnas and decorative elements made of gypsum plaster found in the Hall of the Kings a), the Court of the Lions b) and the Mexuar c), at the Alhambra in Granada (Spain). Close-up view of an example of decayed ornamental plasterwork d).

cement, plasters, and mortars by implementing natural organic additives, such as oils, animal glue or plant extracts, providing enhanced properties (e.g., hydro-repellency or greater mechanical strength).[22–24] In this context, gypsum-derived materials have also played a pivotal role in the evolution of architecture. Being processed through pyrotechnology since the Neolithic (12000–2000 B.C.), alongside lime gypsum has been employed as one of the most important hydraulic binders by subsequent civilizations, such as Ancient Egypt (3100–30 B.C.), Greece (800–146 B.C.), and Rome (753 B.C.–476 A.D.).[25–28] However, the most notable architectural expression in the use of gypsum was reached during the Islamic Golden Age (7th – 13th century A.D.). Since then, the Alhambra of Granada has remained the apex of this architectural style (**Figure 1**a,b).[29–32]

Despite its widespread use and historic importance, gypsum has limited wet-mechanical strength and relatively high solubility, making it prone to deterioration when exposed to humid environments and/or to severe climate changes.[33–39] Due to these handicaps, numerous original architectural elements and ornamental plasterworks from monumental sites suffer from decay (Figure 1c,d). For this reason, several conservation procedures have been recently developed and implemented. A relevant example is the product designed and patented by Rubio-Domene (i.e., Mortero Alhambra),[31,40] where a fluorescent copolymer is mixed with bassanite, quicklime, or calcium carbonate powder in order to obtain luminescent conservation gypsum plasters or lime mortars and stuccoes, allowing to identify and locate recent conservation interventions under UV light. Despite the advances in technology for the elaboration of replicas and material replacement, the use of consolidants is necessary in many conservation interventions in order to improve the mechanical cohesion of the weathered substrate and preserve the original artwork. However, in the specific case of gypsum plasterwork, research regarding suitable consolidants is very limited.[36]

In this work, we exploited the versatility of bio-inspired processes for the development of fluorescent nano-structured bassanite crystals, which we employed as a fully compatible consolidant for the preservation of decayed historic gypsum plasterworks.[41,42] We investigated the effect of the occlusion of organic (macro)molecules during the crystallization of gypsum. In particular, we selected calcein (i.e., a xanthene fluorescent chelating agent with a specific affinity for divalent cations) to study its effect on the morphology, chemical, and optical properties of gypsum crystals from both fundamental and applied perspectives. To this end, we first determined the role of this organic additive during the homogeneous (pre)nucleation of calcium sulfate from solution and the subsequent crystal growth processes. These results allowed us to describe the interaction mechanism

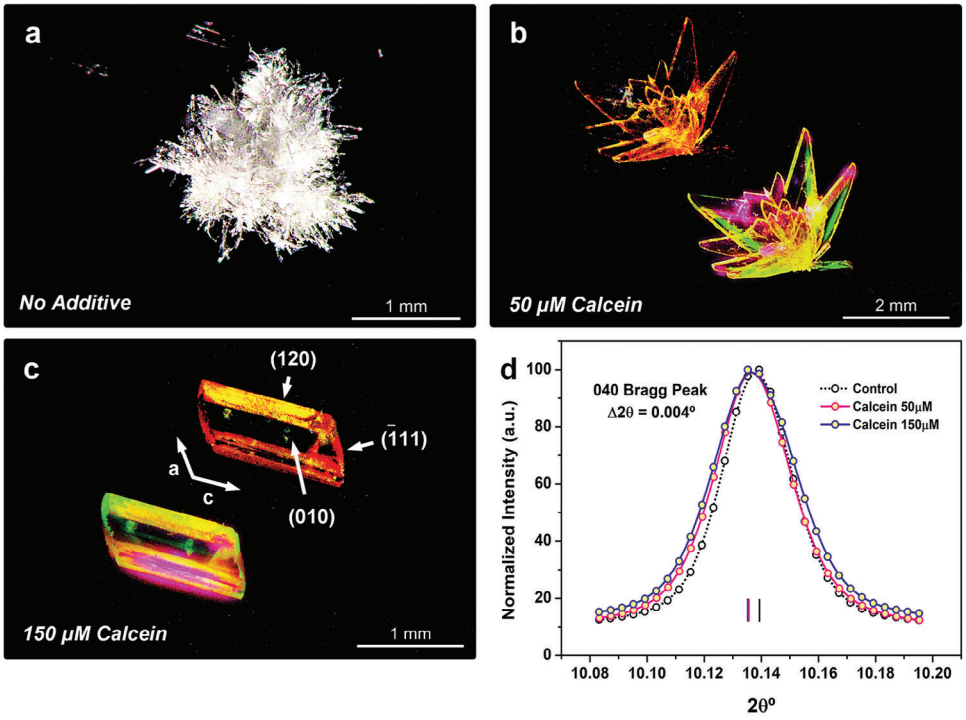

Figure 2. Optical microscopy images under UV light a, b, and c) and HR-XRD patterns (d) of gypsum microcrystals grown in the presence of different calcein concentrations. Vertical color bars in panel d) indicate the position of the point of maximum intensity corresponding to the 040 Bragg peak of each sample (black line, **GG**; red line, **GC-50**; blue line, **GC-150**).

between calcein and the structural growing units involved in the formation of gypsum, which led to important changes in the final crystal habit and physicochemical properties.

In this case, the incorporation of calcein into bassanite nano-consolidants provides a complementary solution for the conservation of plasterwork. In extremely low doses, calcein does not affect the appearance in the visible spectrum neither before nor after the hydration of fluorescent nano-bassanite, a critical issue in heritage conservation. However, when excited with UV radiation, the fluorescent consolidant exhibits an intense green luminescence, allowing conservators to precisely identify areas where the new material is deposited, as well as its penetration depth. This breakthrough enables targeted and accurate conservation applications, preventing under- or over-consolidation and ensuring the preservation of historical artwork. We also demonstrated that calcein modifies crystal growth upon nano-bassanite hydration and the resulting gypsum structure, which presented enhanced weathering resistance. These features are pertinent for the effective consolidation of decayed historical gypsum plasterworks.

2. Results and Discussion

2.1. Growth of Fluorescent Gypsum

Significant variations in the size and morphology of gypsum crystals were detected with increasing additive concentrations when directly precipitated from aqueous solution in the presence of calcein. This additive rendered them fluorescence, as shown by optical microscopy observations with UV light illumination (**Figure 2**; Figure S1b, Supporting Information). In the absence of calcein, numerous micrometer-sized gypsum crystals formed in less than 30 min after mixing the solutions. These crystals showed spherulitic fibro-radiated habits and multiple misalignments along the morphological *c*-axis direction (Figure 2a). Conversely, in the presence of 50 µM calcein **(GC-50)**, flower-like, thin gypsum twinned micro-crystals with "spearhead" or "swallowtail" shapes (i.e., twin law ($\bar{1}01$)),[43] measuring ≈1.5–2.2 mm in size were observed. These crystals, however, were obtained ≈8 h after the solutions were mixed and exhibited well-developed (010) faces (Figure 2b). In contrast, 150 µM calcein **(GC-150)** led to idiomorphic gypsum crystals with sizes of ≈0.8–1.1 mm and no apparent twinning (Figure 2c). These crystals were obtained ≈72 h after the mixing process. These results evidence that calcein, even when dosed in very small amounts, had a marked effect as a crystallization inhibitor, significantly delaying crystal precipitation. In addition, calcein strongly modified the morphology and texture of gypsum precipitates, suggesting that it also acted as a crystal growth modifier. Importantly, the strong and homogeneous fluorescence of gypsum crystals formed in the presence of calcein (Figure 2b,c) points to the occlusion of this additive in the gypsum crystal structure.

Standard powder X-ray diffraction (XRD) analysis provided supporting evidence for these macroscopic observations (Figure S1c, Supporting Information). Crystals precipitated without calcein exhibited intense $\bar{1}21$, 121, $\bar{1}41$, and 022 Bragg peaks, corresponding to well-developed (0*kl*) and (*hkl*) faces. In contrast, **GC-50** crystals exhibited intense 020 and 040 peaks,

corresponding to well-formed (0*k*0) faces, and low intensity $\bar{1}21$, 200, and 062 reflections that suggested poorly developed (*hkl*) faces. **GC-150** crystals displayed intense 0*k*0 reflections and moderately intense $\bar{1}21$, 200, and 062 Bragg peaks, confirming the tendency of gypsum crystals to adopt the equilibrium morphology under these experimental conditions.[44] Inoue and Hirasawa demonstrated the variability of gypsum morphology following precipitation in the absence and presence of several additives, including poly-(acrylic acid) and sodium carboxymethylcellulose, by analyzing the relative intensities of the main diffraction peaks of such crystals.[45] They concluded that crystal growth was suppressed along the [001] direction by organic additives having carboxyl groups, thus leading to a substantial change in morphology and a decrease in the aspect ratio from needle-like, to plate-like and granular gypsum microcrystals, in accordance with the increase in the relative intensity of the 021, 041 and $\bar{2}21$ Bragg peaks. For the highest calcein concentration tested (i.e., 250 µM; **GC-250**) only a scarce granular powder was observed after over ≈2 weeks, and the final phase detected was still gypsum.

Synchrotron high-resolution powder XRD analysis (HR-XRD) revealed a left shift in the position of the 0*k*0 Bragg peaks of gypsum samples containing calcein (i.e., increase in d_{0k0}-spacing), as compared to a calcein-free reference geologic gypsum **(GG)** (Figure 2d). The calculated lattice strain fluctuations ($\Delta b/b$) were 3.841×10^{-4} and 4.078×10^{-4} for **GC-50** and **GC-150** gypsum samples, respectively. This indicates that intracrystalline occlusion of calcein, which was evidenced by fluorescent light microscopy, resulted in a slight structural distortion that only affected the dimension of the *b* lattice parameter (no peak shift was observed in the case of *h*00, *h*0*l*, or 00*l* reflections, showing no lattice strain associated with the *a* and *c* lattice parameters). It has been widely reported that incorporation of macromolecules (e.g., proteins) in biominerals (e.g., calcite and aragonite in mollusk shells) and their biomimetics typically results in anisotropic lattice distortion disclosed by Bragg peak shifts in HR-XRD patterns.[5,10,11,22,46–48] It has been reported that the incorporation of large macromolecules, micelles, and/or nanoparticles might not result in lattice strain.[42,48] In the case of calcein, possibly due to its large molecular size and/or steric constraints, occlusion did not result in large lattice distortion manifested by marked peak shifts, as also observed in the case of calcein incorporation within calcite and aragonite.[42] For lattice modification to occur, the guest molecules have to replace specific ions (i.e., as a "solute") in a homogeneous and systematic way as to achieve long range order.[10] In this case, considering that calcein interacts with Ca^{2+} through strong electrostatic bonds, the slight distortion of the *b* lattice parameter was most likely due to adsorption and incorporation of calcein on the {010} planes,[49] and/or by non-homogeneous replacement of water molecules and/or sulfate groups by calcein during crystallization.

Furthermore, local strain fields around the occluded molecules can cause peak broadening and asymmetry.[50] Here, we observed these effects (Figure 2d) leading to a reduction in crystallite size and an increase in microstrain fluctuations (i.e., D_{0k0},D_{00l}, D_{h00} and η, respectively, as calculated using the Williamson-Hall method; Figure S2a–c, Supporting Information), which provides further evidence of the intracrystalline occlusion of calcein. The calculated lattice strain, as well as the crystallite size and microstrain fluctuation values for **GC-50** and **GC-150** as compared to **GG** are presented in **Table 1**, and also summarized in Figure S3 (Supporting Information).

UV-Vis spectrophotometry analyses of bleached (to eliminate any adsorbed additive) and then dissolved fluorescent crystals enabled the determination of the intracrystalline calcein content in the different gypsum samples (see Experimental Section; Figure S3 and Table S1, Supporting Information). For **GC-50** and **GC-150**, the intracrystalline additive net content was $5.148 \cdot 10^{-4}$ µmol mg^{-1} and $8.997 \cdot 10^{-4}$ µmol mg^{-1}, respectively. Additionally, powders precipitated with 250 µM calcein exhibited an additive net content of $1.527 \cdot 10^{-3}$ µmol mg^{-1}. These results demonstrate significant and dose-dependent occlusion of calcein within gypsum crystals, thus explaining their UV fluorescence and the observed structural effects (Figure 2). They are also relevant for potential biomedical applications, including controlled drug-delivery, as they demonstrate that occlusion of organic molecules of small-to-medium sizes is feasible in a biocompatible mineral phase like gypsum.[51,52]

2.2. Non-Classical Crystallization Mechanism of Calcein-Loaded Gypsum

From a fundamental nonclassical crystallization perspective, it is widely acknowledged that additives (whether organic or inorganic) can significantly impact the different pre- and post-nucleation events that take place during the precipitation of pure mineral phases.[23,53–56] This is a promising strategy for the design of materials with tailored morphologies, physical-chemical properties, and, therefore, technical applications. In line with this, and because we aimed to develop and test a novel bio-inspired functional (i.e., fluorescent) and fully compatible consolidant for the conservation of deteriorated historical gypsum plasterwork, we first assessed the effect of calcein during the early stages of gypsum crystallization (i.e., pre- and post-nucleation stages).

Potentiometric titration was employed to study the evolution of $[Ca^{2+}]_{free}$ during the pre-nucleation, nucleation, and post-nucleation stages of calcium sulfate in both the absence and presence of the fluorescent additive (**Figure 3**). In order to provide a precise depiction of the interaction mechanism between calcein and Ca^{2+}, the titration curves were segmented into 3 sections: I) pre-nucleation stage, II) nucleation stage, and III) post-nucleation stage (i.e., particle growth).

During the pre-nucleation stage, the measured $[Ca^{2+}]_{free}$ consistently remained lower than the total dosed Ca^{2+}. According to Gebauer et al.,[57,58] this phenomenon indicates the stabilization of pre-nucleation clusters (PNCs), which are described as polynuclear associates that typically precede the formation of more complex condensed phases, such as liquid precursors and/or amorphous solids. The concentration-dependent stabilization of PNCs by calcein was demonstrated by the increase in $[Ca^{2+}]_{bound}$, as shown by a flattening of the slope of the $[Ca^{2+}]_{free}$ versus time curves during the pre-nucleation stage as compared with the control curve. This effect of PNC stabilization has been extensively documented in other systems (e.g., $CaCO_3$-H_2O) for other carboxylate-rich organic additives, such as poly(acrylic acid (PAA), poly(aspartic acid) (PASP), citric acid and several

Table 1. Summary of calculated lattice parameter ***b***, lattice distortion, crystallite size, and microstrain fluctuations for GC-50 and GC-150 as compared to geologic gypsum (GG). *For the crystallite size and microstrain fluctuation (obtained using the Williamson-Hall plot method), the error is indicated as the standard deviation (σ).

	b	$\Delta b/b$	D_{0k0} [nm]	D_{00l} [nm]	D_{h00} [nm]	η
GG	15.20441 ± 0.00013	–	166.17 ± 0.04	110.24 ± 1.71	99.28 ± 0.78	0.00120 ± 0.00010
GC-50	15.21025 ± 0.00011	3.841×10^{-4}	151.29 ± 0.54	97.86 ± 0.24	87.57 ± 0.57	0.00125 ± 0.00004
GC-150	15.21061 ± 0.00012	4.078×10^{-4}	146.41 ± 0.39	88.11 ± 0.43	78.11 ± 0.68	0.00148 ± 0.00005

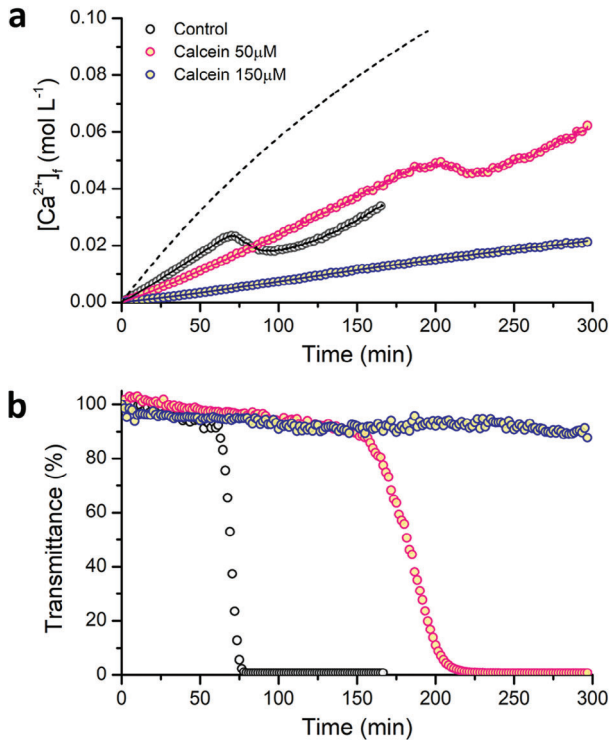

Figure 3. Time development of the free Ca^{2+} concentration a) and transmittance b) during gypsum precipitation experiments in the absence (black dots, control) and presence of calcein (red dots, 50 μM; blue dots, 150 μM), in comparison with the total dosed Ca^{2+} concentration (dashed line).

polysaccharides,[59–62] but its implications in the $CaSO_4$-H_2O system are relatively unexplored.

As we moved along the reaction coordinate, $[Ca^{2+}]_{free}$ exhibited a linear increase as Ca^{2+} was dosed until a point where the slope decreased, followed by a sudden drop in $[Ca^{2+}]_{free}$, indicating the nucleation of the first solid particles. Calcein, as observed in the initial bulk crystallization experiments, inhibited crystallization, even at exceedingly low additive concentrations. This inhibitory effect was evidenced in the titration experiments by a significant delay in the nucleation of the first $CaSO_4 \cdot nH_2O$ particles. In the presence of 50 μM calcein, the induction time for nucleation increased 2.7 times as compared to the control. The impact of calcein became more apparent as the additive concentration increased to 150 μM, where complete inhibition of nucleation was observed. Even after more than 10 h, no visible precipitates were observed. As previously reported by Nicoleau et al.,[63] organic additives (e.g., PAA) inhibit the nucleation of gypsum by hindering collisions between PNCs, which in turn decreases their attachment probability and increases their kinetic persistence in solution.

Calcein has a strong affinity for divalent cations and behaves as a bidentate chelating agent similar to EDTA (with 4 carboxylic groups deprotonated at pH < 6; $pK_{a1} = 2.1$, $pK_{a2} = 2.9$, $pK_{a3} = 4.4$, $pK_{a4} = 5.5$; and 2 tertiary amine groups). Thus, it is reasonable to infer that the complexation of Ca^{2+} may have potentially played a role in the nucleation and growth mechanisms. The complexation of Ca^{2+} by calcein was demonstrated by the delay in the initial increase of measured $[Ca^{2+}]_{free}$ at the beginning of the titration experiments (Figure S4, Supporting Information). Specifically, $[Ca^{2+}]_{free}$ started increasing only once the complexation capacity of the additive was reached. In titrations using 50 μM calcein, the complexation delay with respect to the control curve (i.e., elapsed time from probe stabilization to $[Ca^{2+}]_{free}$ initial increase) was ≈0.8 min, while in the presence of 150 μM calcein, this delay was extended to ≈2.2 min, indicating a concentration-dependent effect on the initial complexation process. Nevertheless, the observed inhibitory effect cannot be solely attributed to Ca-calcein complexation. This is so because the total molar concentration of the additive was orders of magnitude lower than the total added Ca^{2+} during the titration experiments. Moreover, it is expected that most of the calcein would be coordinated to Ca^{2+} at the very beginning of the experiment.[64] Ultimately, the possible inhibitory effect of Ca^{2+} complexation can be disregarded at such low additive concentrations.

We also analyzed the events that occur near the nucleation onset by comparing the evolution of $[Ca^{2+}]_{free}$ with the corresponding transmittance measurements. In control runs, the transmittance suffered a sudden drop, which however, preceded (by ca. 15 min) the sudden decrease in measured $[Ca^{2+}]_{free}$ marking the nucleation and subsequent growth of the initial calcium sulfate particles. This decoupling between the drop in transmittance and the $[Ca^{2+}]_{free}$ decrease was more evident in calcein-including runs. In the presence of 50 μM calcein, the measured transmittance decreased gradually before reaching the nucleation onset marked by the drop in measured $[Ca^{2+}]_{free}$. This suggested that both in the control run and, especially, in the presence of calcein, the initial stage of nucleation occurred following a liquid-liquid phase separation, where a dense liquid phase (most likely made up of highly hydrated PNCs) separates from a less concentrated solution, as observed in other systems.[65] However, this possibility must be carefully evaluated using more advanced techniques, such as SAXS and/or analytical ultracentrifugation. Finally, as discussed above, higher concentrations of calcein led to complete nucleation inhibition, resulting in no discernible change in transmittance throughout the time course of these experiments.

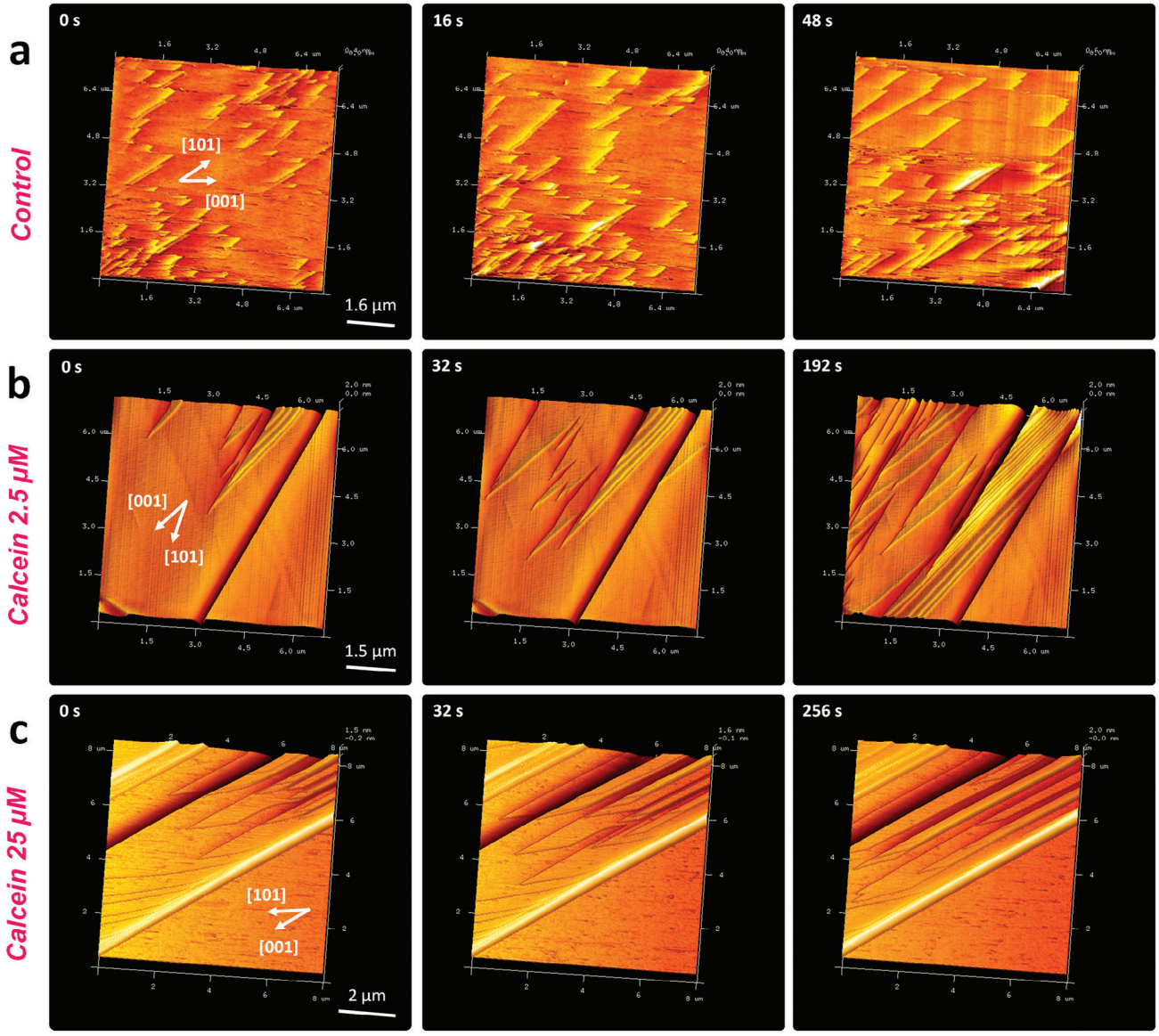

Figure 4. Time sequence of AFM deflection images of {010} cleavage surfaces of gypsum crystals obtained following growth in the absence a) and presence of 2.5 and 25 µM calcein b and c). Growth directions [001] and [101] are indicated by arrows.

In situ, fluid-cell AFM observations conducted on gypsum {010} cleavage surfaces, both in the absence and presence of calcein, revealed a pronounced modification of anisotropic step propagation kinetics by this additive. Specifically, the introduction of calcein led to a discernible alteration in growth dynamics at the nanoscale. During control experiments conducted without the additive (**Figure** 4a; Video S1, Supporting Information), the rapid emergence of multiple steps aligned with the [101] and [001] directions was observed, followed by their advancement and a swift step-bunching after approximately 16 s. This implies that growth by ion adsorption along the *a*- and *c*-axis directions was not impeded. Note that gypsum grows extremely fast, even at low saturation index values (i.e., $SI = log(IAP/K_{sp})$, being IAP the ion activity product and K_{sp} the solubility product of the relevant phase; see Experimental Section). Although we decided to increase the scan rate by compromising image quality, in the absence of calcein growth rates could not be accurately measured. In the presence of 2.5 µM calcein, the growth rate (i.e., velocity of step advancement) along the *c*-axis direction sharply decreased, and was almost completely inhibited along the *a*-axis direction (Figure 4b; Video S2, Supporting Information). This also resulted in a reduction of the step-bunching effect. Increasing the concentration of calcein by an order of magnitude (i.e., 25 µM) resulted in much slower growth kinetics than in the previous cases (Figure 4c; Video S3, Supporting Information).

Considering the morphological evolution of gypsum crystals obtained at different calcein concentrations (i.e., spherulitic → arrowhead → idiomorphic), our hypothesis is that the adsorption of calcein onto each dominant face of the gypsum structure

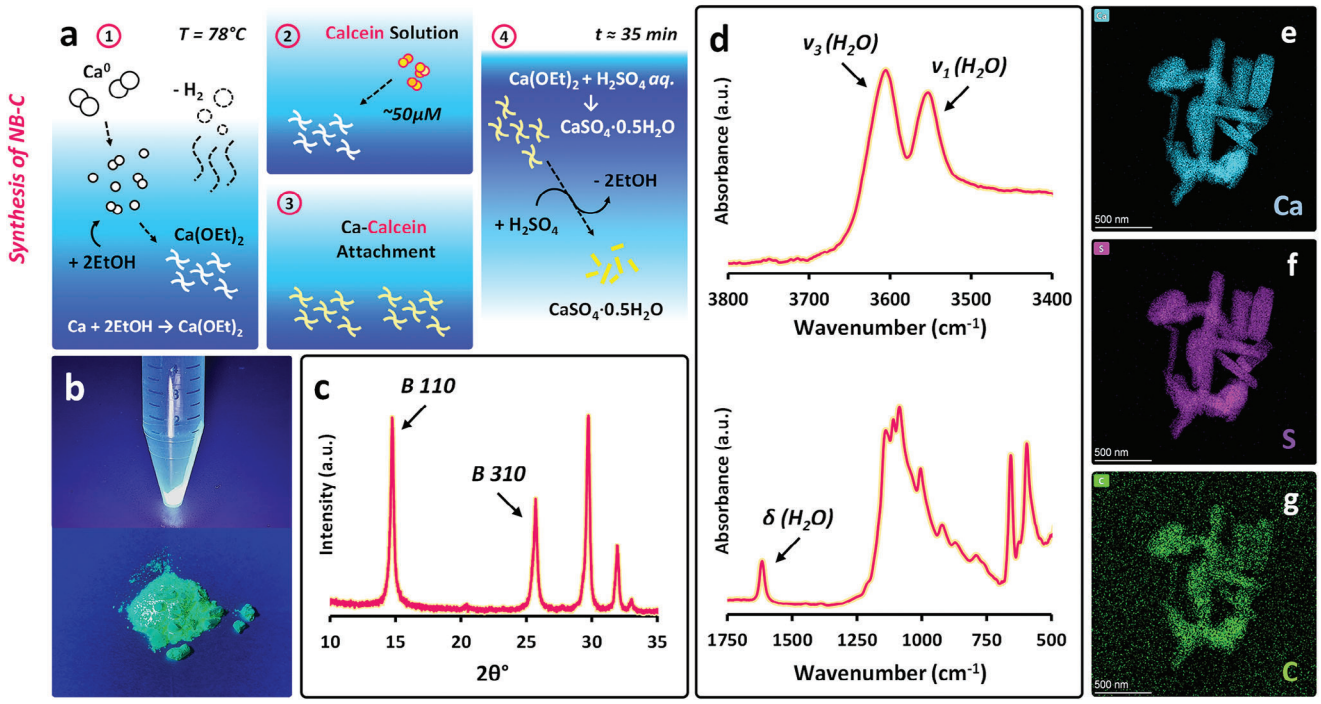

Figure 5. Synthesis a and b) and characterization c–g) of fluorescent nano-bassanite (NB-C). XRD pattern c), FTIR spectrum d) and EDX elemental mappings e–g) show that the obtained product is phase-pure bassanite, which also contains calcein.

(i.e., {010}, {120}, and {$\bar{1}$11}; Figure 2) results in the inhibition of crystal growth, regardless of their relative stability (i.e., interfacial free energy). Note that, for example, if poisoning by the organic additive occurs on the {010} surfaces, growth by ion addition in the *b*-axis direction would be impeded, but it is still viable along the *a*- and *c*-axis directions, resulting in large area (010) faces. Increasing calcein concentration leads to a more exaggerated situation of the same inhibitory effect so that gypsum crystals showing equilibrium morphologies can be obtained even under high supersaturation conditions. These observations regarding macroscopic morphology correlate well with AFM measurements and are in accordance with the recorded conventional XRD patterns of gypsum crystals grown both in the absence and presence of calcein dosed at different concentrations. They are also congruent with the HR-XRD results. The slight lattice distortion along the *b* direction due to intracrystalline calcein is consistent with surface adsorption of calcein molecules on {010} faces followed by their occlusion by advancing growth steps.[49] Indeed, adsorption followed by occlusion seems to be the predominant interaction mechanism between calcein and the growing gypsum, ultimately leading to morphology variations.

Understanding how calcein modifies the crystallization pathway of gypsum from solution and its physicochemical properties was crucial for the later design of novel $CaSO_4{\cdot}nH_2O$ nanoconsolidants. It is important to mention that bassanite is the direct precursor of gypsum plasters, which are widely used as construction and ornamental materials. For this reason and because we also aimed to produce novel consolidants for the conservation of plasterworks, we synthesized fluorescent bassanite nanoparticles and evaluated the behavior of calcein during their transformation into gypsum cement (see below).

2.3. Synthesis and Characterization of Fluorescent Nano-Bassanite

Nano-bassanite was synthesized in the absence or presence of calcein following the solvothermal method by Burgos-Ruiz et al.[66] Details of this solvothermal synthesis are presented in the Experimental Section. **Figure 5a** schematically shows the different steps of such a synthesis route, whereas Figure 5b shows the final product synthesized in the presence of calcein (50 μM; see details in the Experimental Section), which is fluorescent under UV light.

XRD analysis (Figure 5c) revealed that the synthesis product **(NB-C)** was phase-pure monoclinic bassanite (space group *I2*). Furthermore, FTIR spectra (Figure 5d) showed moderate intensity bands at 3554 and 3610 cm^{-1}, corresponding to the ν_1 asymmetric and ν_3 antisymmetric O-H stretch vibrations, along with the moderate intensity δ OH bending band at 1618 cm^{-1}, corresponding to structural water in bassanite. In the fingerprint region, we observed a quadruplet at 1010, 1086, 1108, and 1137 cm^{-1}, along with a doublet at 595 and 660 cm^{-1}, corresponding to the ν_1–ν_4 stretching vibration modes of SO_4 groups. We also observed low-to-moderate intensity bands ranging from 694 to 941 cm^{-1} that were ascribed to the incorporated calcein. Note that the main IR absorption bands (i.e., corresponding to C-O, C-H, and C = C bonds) of calcein overlap with the stretching modes of SO_4 groups and could not be properly identified.

The UV-Vis analysis of dissolved **NB-C** (Figure S3 and Table S1, Supporting Information) further confirmed the presence of the additive in the nano-bassanite crystals and revealed a calcein net content of 4.81×10^{-4} μmol mg^{-1} (Table S1, Supporting Information).

TEM analysis (Figure S6a, Supporting Information) showed that the synthesized product consisted of nano-crystalline rod-like bassanite aggregates. This observation is supported by their SAED pattern exhibiting diffraction spots corresponding to the 114, $\bar{3}14$, 334, and 240 reflections (Figure S6a inset, Supporting Information). The particle equivalent length, measured along the *c*-axis direction, ranged from 90 to 500 nm, with widths measured along the *a* or *b* directions ranging between 40 to 80 nm. More importantly, S/TEM EDX elemental mappings (Figure 5e–g) and spectra (Figure S6b, Supporting Information) were decisive in proving that calcein was evenly distributed inside the bassanite nanocrystals, as confirmed by the elemental carbon map.

2.4. The Hydration Mechanism of Fluorescent Nano-Bassanite

The synthesized **NB-C** particles were subjected to hydration at room *T* in a high relative humidity atmosphere (RH > 90%) for at least 2 weeks to obtain partially hydrated bassanite (i.e., a mixture of bassanite and gypsum). TEM analyses showed that the newly formed gypsum grew by epitaxy along the *c*-axis direction of the pre-existing bassanite nanocrystals (**Figure 6**a). Importantly, EDX elemental mapping confirmed that calcein was still present in the structure of gypsum formed after bassanite hydration (Figures S7 and S8, Supporting Information). De Yoreo et al.,[67] have previously shown that the low-energy interfaces of bassanite faces along the *c*-axis direction promotes the heterogeneous nucleation and growth of gypsum in solution. Note, however, that we did not use liquid water to promote the hydration of bassanite. Instead, deliquescence on the surface of the hemihydrate was the primary source of water in our experimental setup. Moreover, we observed that the diffuse diffraction spots corresponding to the SAED pattern of the tip of individual hydrated bassanite nanocrystals were elongated along the [001] direction (i.e., long axis and growth direction), showing Bragg reflections with a marked broadening, whereas those corresponding to newly formed gypsum also showed broadening and significant arcing (≈8–12°) (Figure 6a–c). As previously discussed, these effects are likely caused by the presence of structural defects, microstrain, and reduced crystallite size, compatible with the incorporation of calcein in the structure of both nano-bassanite and the newly-grown gypsum.

Interestingly, during TEM analyses we also observed small amorphous structures resembling liquid-like fractals of nanodroplets (Figure 6d–f). EDX analyses and mappings revealed the presence of elemental Ca and S (Figure 6g–i), suggesting the formation of an amorphous calcium sulfate (i.e., ACS) phase during the hydration of **NB-C**. These amorphous structures were extremely sensitive to the electron beam, which is indicative of a high degree of hydration. Recently, Ilett et al.,[68a,b] have detected similar ACS structures in samples prepared by cryogenic quenching and vacuum sublimation of 50 mM $CaSO_4$ solutions (in the absence of additives) using high-resolution TEM. We further analyzed cryo-quenched aliquots of supersaturated $CaSO_4$ solutions where PAA was used as a proxy for calcein, under full Cryo-TEM and normal TEM analysis conditions after eliminating the formed frost by vacuum sublimation (i.e., plunge-freezing and vacuum sublimation, PFVD; see Experimental Section) (Figure 6h–i; Figure S9, Supporting Information). Note that, in essence, carboxylate-rich organic additives, whether monomeric or polymeric (e.g., calcein and PAA), function as nucleation inhibitors by sequestrating Ca^{2+} and stabilizing PNCs and/or amorphous precursors (e.g., amorphous calcium carbonate, ACC).[69,70] In the presence of PAA, we observed individual globular amorphous structures with the same dimensions as the nanodroplets that conform the previously shown fractal structures.

Our hypothesis is that these ACS fractals were formed following a diffusion-limited colloidal aggregation mechanism.[71] This evidence supports the idea that the amorphous structures we observed were not artifacts resulting from sample preparation. It also proves the existence of a highly hydrated transient ACS phase during the bassanite → gypsum transition, which must be the same, or at least very similar in nature, as the widely reported ACS species that precedes the direct formation of gypsum from solution.[72–75]

These results showed that the bassanite → gypsum phase transition occurred via a non-classical dissolution-precipitation mechanism, described as follows: I) under atmospheres with high water vapor partial pressure, water is able to condensate on the surfaces of bassanite crystals, thus enabling their partial dissolution;[76] II) the resulting solution is supersaturated with respect to gypsum and also contains calcein, which stabilizes PNCs and, subsequently, highly hydrated transient ACS nanodroplets; III) the formation of fractal structures of ACS occurs through diffusion-limited colloidal aggregation; IV) mass transport and heterogeneous precipitation of ACS occurs on the tips of the pre-existent bassanite crystal, and after an amorphous-to-crystalline phase transition, the new calcein-loaded gypsum (i.e., the most stable $CaSO_4{\cdot}nH_2O$ phase under standard *P* and *T* and humid conditions) grows epitaxially along the [001] direction of bassanite.

Note that the hydration of bassanite to form gypsum is the main chemical process leading to the setting, cementation, and hardening of gypsum-based building materials, and it is, in fact, the reason why we focused on producing organic-modified bassanite nanomaterials. Below we further discuss the specific implications of fluorescent nano-bassanite hydration in the field of heritage conservation.

2.5. Resistance to Dissolution

One major issue regarding gypsum-based building and decorative materials is their relatively high solubility (i.e., gypsum solubility ≈2.5 g L^{-1} at 25 °C), especially in environments with marked and cyclical humidity variations. For this reason, we evaluated the effect of the intra-crystalline calcein in fully hydrated **NB-C** particles on their dissolution kinetics, as compared to both geologic gypsum **(GG)** and a non-functionalized hydrated nano-bassanite **(NB)** control. Through bulk dissolution experiments in milli-Q grade deionized water (pH ≈6.25, $T = 25$ °C) we analyzed the time variation of $[Ca^{2+}]_{free}$ (**Figure 7**). We observed that the dissolution rate of the hydrated **NB-C**, calculated as apparent dissolution rate constants, was lower ($k_{NB\text{-}C} = 1.315 \times 10^{-4}$) than those of the non-functionalized controls ($k_{GG} = 1.878 \times 10^{-4}$; $k_{NB} = 1.808 \times 10^{-4}$).

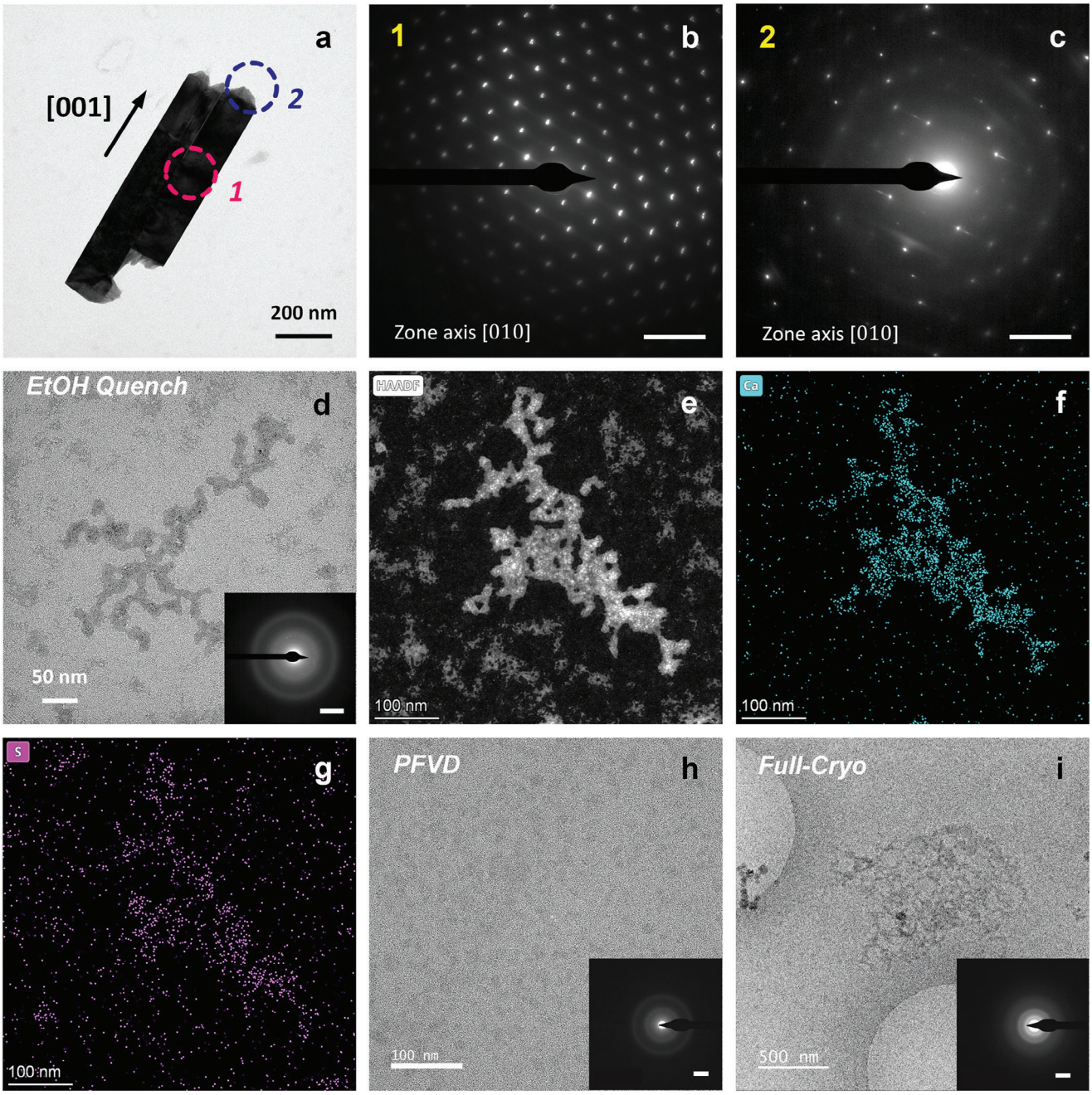

Figure 6. a–c) TEM and SAED analyses of the epitaxial hydration of fluorescent nano-bassanite driven by a coupled non-classical dissolution-precipitation mechanism. d) TEM image of fractal-like structures made up of nanodroplets (transformed into ACS during EtOH quenching and drying) observed during the hydration of calcein-loaded nano-bassanite. e–g) HAADF imaging and corresponding EDX elemental Ca and S mappings corroborate that the observed fractals are amorphous calcium sulfate structures; h, i) TEM and Cryo-TEM images of dispersed nanodroplet (liquid precursor of ACS) formed by direct precipitation of calcium sulfate in the presence of PAA. Note the textural/structural similarity of the individual isolated droplets with those forming aggregated in (d). All scale bars in SAED images correspond to 5 nm^{-1}.

Moreover, in the case of the hydrated **NB-C** sample, the maximum (i.e., asymptotic) $[Ca^{2+}]_{free}$ value reached was lower than that of the non-functionalized controls. In this case, the complexation of Ca^{2+} by calcein might have contributed to a lower measured $[Ca^{2+}]_{free}$. However, the molar amount of occluded calcein is extremely low (ca. 4.8×10^{-8} moles of calcein per 100 mg of fluorescent gypsum; Table S1, Supporting Information) as compared to the total amount of Ca in gypsum (ca. 5.8×10^{-4} moles of Ca per 100 mg of gypsum; Table S1, Supporting Information). For this reason, the decrease in the measured $[Ca^{2+}]_{free}$ and dissolution rate cannot be solely attributed to complexation. It is thus likely that due to the short time-span of the dissolution

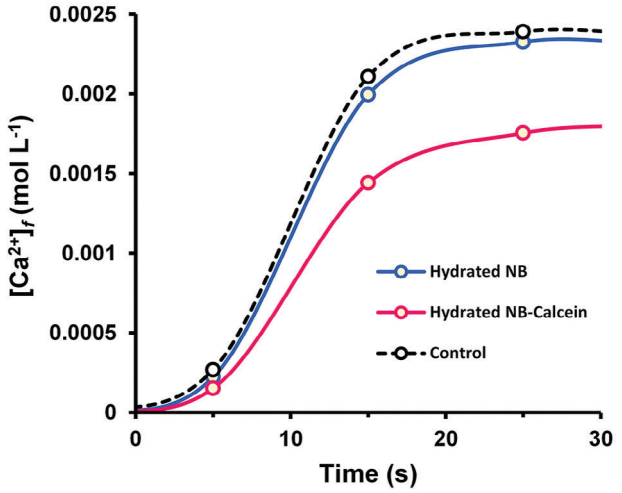

Figure 7. Time variation of the free Ca^{2+} concentration upon dissolution of gypsum formed after hydration of fluorescent nano-bassanite (red line, NB-C) as compared to gypsum formed after hydration of a non-functionalized nano-bassanite control (NB, blue line) and a geologic gypsum (GG, black line).

experiment, the system did not reach equilibrium. Therefore, due to its slower dissolution kinetics, the maximum solubility of calcein-loaded gypsum was not reached.

It is worth mentioning that the occlusion of organics in calcium carbonate biominerals and their biomimetics has been reported to modify not only their physical-mechanical properties but also their resistance to chemical weathering (i.e., dissolution).[22] A similar effect was apparently achieved here by the occlusion of calcein in gypsum crystals formed after the hydration of **NB-C**, explaining the observed reduction in dissolution rates. This effect has strong implications for heritage conservation, as the use of calcein-inclusive nano-bassanite for the consolidation of historical gypsum plasterwork would not only enhance the mechanical resistance of treated substrates (see below) but also increase their weathering resistance.

2.6. Gypsum Plaster Consolidation Using Fluorescent Nano-Bassanite

Cubic plaster mock-ups (prepared by mimicking the historic Islamic gypsum plasters present at the Alhambra; Figure S10, Supporting Information) were sprayed with ethanol dispersions of fluorescent nano-bassanite consolidants (with occluded calcein) on one horizontal face until saturation of the substrate was achieved (see details in the Experimental Section).

To verify the cementation and mechanical reinforcement effects of the produced fluorescent nano-bassanite particles once applied to the plaster substrate and transformed into gypsum, we evaluated the penetration of ethanolic dispersions of the consolidants (5 g L^{-1}) by exposing treated, cured, and vertically fractured gypsum plaster specimens to UV light ($\lambda = 365$ nm). UV irradiation revealed the extent of penetration achieved by the fluorescent nano-bassanite particles, which reached a depth of approximately 4 mm within the porous gypsum plaster samples (**Figure** 8b).

TEM-EDX maps confirmed that calcein was homogeneously distributed inside the initial bassanite nanoparticles and the final gypsum crystals, which is the actual cementing phase obtained upon the hydration of bassanite. The insolubility of this dye in pure ethanol should prevent any desorption from the particle surface if any calcein were not only occluded but also adsorbed. These 2 factors played a pivotal role in ensuring that only the newly incorporated bassanite particles and their hydration product emitted green luminescence, thus providing an effective strategy for easily monitoring the penetration capacity of the consolidant. This is actually a key factor in determining the efficacy of a consolidation treatment. Note also that the luminescence of calcein-containing gypsum would also enable to easily and non-destructively spot consolidated areas once the treatment is applied in situ by simply illuminating the surface with UV light.[77]

Mercury intrusion porosimetry analyses were conducted on treated and cured (i.e., following conversion of bassanite into gypsum) plaster samples (Figure 8c), revealing a 5% reduction in total porosity, as compared to the untreated control (i.e., total porosity of treated and untreated samples being 47% and 53%, respectively). Furthermore, the median volume corresponding to pores with diameters of 7 μm experienced a sharp reduction, accompanied by an increase in the volume of pores with diameters of 2 and 4 μm. This is consistent with the partial filling-in effect of the treatment (i.e., deposition of the newly-formed gypsum cement on the pore walls of larger pores, thereby reducing their diameter).[78] Additionally, these results demonstrated that there was no pore clogging, thereby ensuring that the treated substrate was still able to "breathe", that is, to maintain an appropriate water vapor permeability. This is critical to ensure physical compatibility of this consolidation treatment. Also, the chemical compatibility is fully ensured as both the consolidant and substrate share similar composition and structure (i.e., gypsum).

Drilling resistance measurements (Figure 8d) provided additional evidence for the effectiveness of the nano-bassanite consolidation treatments. The drilling resistance of treated and cured gypsum plaster increased over the first 2 millimeters of the drilling profile, reaching a maximum increment of 1.56 ± 0.23 N (i.e., 279.31% ± 26.44%) as compared with the untreated plasters. This increase in mechanical strength is in good agreement with the reduction in total porosity and with the observed penetrability of the fluorescent consolidation treatment. It is also proof that the transformation of nano-bassanite into gypsum during the curing of the treated samples (a transformation that led to fluorescent gypsum as shown by the UV illumination), resulted in an effective consolidation.

According to the nano-bassanite hydration results discussed above, cementation occurs through the sequential dissolution of bassanite and re-precipitation of gypsum. Because there is gypsum in the treated plasters, the heterogeneous regrowth of gypsum on such pre-existing gypsum crystals is also possible. In both cases, the bassanite → gypsum transition produces a lattice expansion accompanied by an increase in the molar volume, leading to a higher degree of structural compaction.[79]

Consolidation results and the functionalities imparted by calcein demonstrated the potential and efficacy of nano-bassanite as the first fully compatible (chemically and physically) consolidant for decayed gypsum plasterwork. Furthermore, luminescence

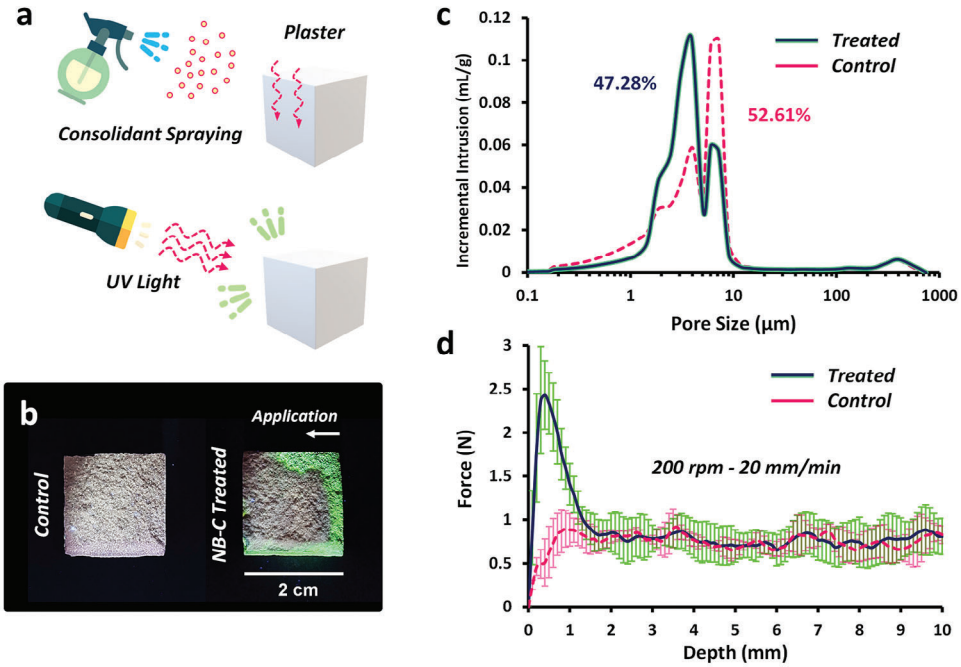

Figure 8. Consolidation treatment of gypsum plaster specimens using ethanolic suspensions of fluorescent nano-bassanite a). Green luminescence under UV irradiation allowed to determine the degree of penetrability of the consolidant (samples were split in half to observe luminescence in their interior) b), which ultimately produced a decrease of the total porosity of the treated plaster as show by MIP results c) and an increase of the drilling resistance d). *Lines in (d) correspond to the calculated average drilling resistance, while error bars correspond to their corresponding standard deviation (σ).

tests carried out 10 months after application of the consolidant showed that the fluorescence of the calcein-modified nano-bassanite resisted chemical degradation after long periods of time (Figure S12, Supporting Information).

3. Conclusion

Our study on the bio-inspired precipitation of calcium sulfate in the presence of calcein shows that this additive is incorporated into the structure of gypsum, affecting the structure, morphology, and physical-chemical properties of this crystalline material.

Through an in-depth analysis of the formation of these luminescent crystals, the obtained results allow us to propose a non-classical multi-step nucleation involving a liquid-liquid phase separation mechanism. In the presence of calcein, and probably other organic additives (e.g., PAA), the formation of gypsum particles is preceded by the stabilization of highly hydrated PNCs, followed by the formation of a dense liquid precursor, and an amorphous solid (ACS).

Analogously, crystal growth is hindered by the adsorption of calcein, on all dominant faces of gypsum. The variations of the growth rates are concomitant with the observed calcein concentration-dependent morphology changes.

The study of the fundamental crystallization mechanism of gypsum in the presence of calcein furthers the knowledge about the hydration and cementation of calcein-loaded nano-bassanite consolidants obtained through a solvothermal synthesis method. In summary, we propose that the bassanite → gypsum phase transition follows a non-classical dissolution-precipitation mechanism: I) In environments with high water vapor partial pressures, water condenses on bassanite crystal surfaces, facilitating partial dissolution. II) PNCs are stabilized by calcein, which leads to the formation of highly hydrated transient ACS nanodroplets in a supersaturated regime. III) Mass transport and heterogeneous precipitation occur on the tips of existing bassanite crystals, with new calcein-loaded gypsum growing epitaxially along the [001] direction.

We also demonstrate that gypsum formed after hydration of calcein-containing nano-bassanite particles show increased dissolution resistance, whereas application of the fluorescent nano-bassanite consolidant to gypsum plaster mock-ups demonstrates excellent penetrability and good mechanical reinforcement. Altogether, we show that this novel consolidation treatment is effective both from a physical-mechanical and chemical point of view, with no detrimental drawbacks.

Ultimately, our work demonstrates the importance of investigating the crystallization and phase transition mechanisms in the $CaSO_4$-H_2O system, from nucleation to crystal growth, and how controlling these processes by including specific additives enables the design of advanced functional materials with tailored properties. In this particular case, we developed an effective consolidant for historic gypsum plasterwork, which offers a fully compatible, facile and controlled strategy for enhancing gypsum plaster durability while enabling real-time monitoring of treatment efficacy. Future research should explore the long-term effectiveness of this conservation treatments, as well as its comparison with other standard consolidation treatments commonly applied in heritage conservation (e.g., nanolimes).

4. Experimental Section

Initial Screening of Calcein Concentration for Morphology Control: Fluorescent gypsum crystals (Figure 2) were obtained by mixing equimolar aqueous solutions of $CaCl_2$ and $(NH_4)_2SO_4$ up to a final Ca^{2+} and SO_4^{2-} concentration of 0.1 M, in the presence of increasing concentrations of calcein (i.e., 0, 50, 150 and 250 µM) on sterile polystyrene crystallization microplates (6 × 4 wells, 3300 µL per well).

Precipitates were set to crystallize for a total of 6 days under lab conditions (see Supplementary Material, Figure S1a, Supporting Information). Note that concentrations greater than 150 µM resulted in scarce gypsum precipitation after extremely long induction times (weeks). This is why here the results for calcein concentrations up to 150 µM were consistently reported.

Finally, precipitates were collected, dispersed in 96° ethanol, and sonicated for 2 min in order to eliminate any interference of residual calcein adsorbed onto crystal surfaces.

Modulating Phase Selectivity in $CaSO_4{\cdot}nH_2O$: With the goal of achieving phase-pure bassanite ($CaSO_4{\cdot}0.5H_2O$) production, the anti-solvent effect of ethanol on the homogeneous precipitation of $CaSO_4{\cdot}nH_2O$ phase was investigated. It is worth noting that diverse strategies to induce bassanite formation have been described, involving precipitation under conditions of high ionic strength, temperature, and/or the presence of organic additives.[80] While these methodologies generally share a common principle (i.e., reducing water activity and inducing supersaturation by modifying the solvation sphere enveloping ions to lower the interfacial energy barrier required for the liquid-solid phase transition) the selection of the anti-solvent approach was motivated by its ability to circumvent the interference of excessive secondary electrolytes or the need for using additives other than calcein.

To accomplish this, a series of homogeneous precipitation experiments, involving the dropwise addition of a 0.3 M $CaCl_2{\cdot}2H_2O$ hydroalcoholic solution, preloaded with 50 µM calcein, into a 0.1 M $(NH_4)_2SO_4$ hydroalcoholic solution was conducted (Figure S5a–b, Supporting Information). Various ethanol-to-water ratios were employed (i.e., 50%, 80%, and 90% vol./vol. EtOH/H_2O). Note that in 0.1 M hydroalcoholic solutions, and under standard conditions, the solubility limit for $(NH_4)_2SO_4$ is approached at ≈90% vol./vol. ethanol-to-water ratio.

It is important to highlight that, despite the miscibility of water and ethanol as solvents, calcein remains insoluble in ethanol. This aspect is relevant for the design of fluorescent nano-bassanite consolidants, particularly with regard to their intended dispersion in absolute ethanol for practical conservation applications. Note that ethanol enables the formation of stable nano-bassanite dispersions, and once applied to a substrate this solvent rapidly evaporates without leaving any residue. Ethanol also prevents the early hydration of (nano)bassanite, as could occur in aqueous dispersion, thereby preventing pore-clogging during conservation applications.

Under the described experimental conditions, independently of the ethanol-to-water ratio, a fluorescent solid phase precipitated instantaneously after the addition of each drop of the calcein-loaded $CaCl_2$ hydroalcoholic solution was observed (Video S4, Supporting Information). Examination of the obtained solids via XRD and FTIR analysis (Figure S5c,d, Supporting Information) unveiled that this hydroalcoholic precipitation route led to the co-precipitation of bassanite alongside gypsum. While gypsum dominated as the primary product at a 50% ethanol content, the proportion of precipitated bassanite increased with ethanol content exceeding 80%. This was shown by the increased intensity of the 110 and 114 Bragg reflections corresponding to bassanite, concomitant with a diminishing intensity of the 020 Bragg peaks corresponding to gypsum.

Additionally, significant variations were evident in the FTIR spectra, specifically in the O-H stretching (ν_1, H_2O) and bending (δ_1, H_2O) vibration modes associated with structural water. A notable increase in the intensity of the shoulder detected at 3604 cm^{-1} in the stretching region, corresponding to bassanite, was identified for solids obtained employing an ethanol content higher than 80%, congruent with the X-ray diffractograms.

Synthesis of Phase-Pure Fluorescent Nano-Bassanite: Considering that phase pure fluorescent (nano)bassanite using hydroalcoholic solutions can not be obtained, which could latter on be used for the consolidation of gypsum plasterwork, an alternative solvothermal route was explored.

Phase-pure fluorescent bassanite nanoparticles were synthesized through a modification of a patented solvothermal pathway, as outlined elsewhere.[50] This method involves the generation of amorphous calcium ethoxide, followed by its subsequent reaction with sulfuric acid, described by the ensuing reactions (Figure 5a):

$$Ca^0 + 2C_2H_5OH \rightarrow Ca(OC_2H_5)_2 + H_2 \quad (1)$$

$$Ca(OC_2H_5)_2 + 2H_2O \rightleftarrows Ca(OH)_2 + 2C_2H_5OH \quad (2)$$

$$Ca(OH)_2 + H_2SO_4 \rightarrow CaSO_4 \cdot 0.5H_2O + 1.5H_2O \quad (3)$$

As a first step (Equation 1), a concentrated suspension of calcium ethoxide is obtained through the complete, irreversible oxidation of 2 g of metallic calcium in 200 mL of absolute ethanol with the formation of H_2 (g). This process is carried out under reflux condensation at ≈78 °C, under anhydrous conditions for a minimum of 6 h. Afterward, 70 mL of anhydrous toluene was introduced into the reaction mixture. At this moment, 4 mL of a 2.5 mM aqueous calcein solution was added (≈50 µM final calcein concentration). To ensure Ca-Calcein interaction, the mixture is stirred for approximately 5 min. During this stage, the precipitation of $Ca(OH)_2$ is initiated through the hydrolysis of calcium ethoxide upon the addition of the calcein solution (Equation 2). The third step comprises the drop-wise addition of 10 mL of a 5 M H_2SO_4 solution, which induces rapid acid-base neutralization (Equation 3). Note that, under these conditions, the total water content is less than ≈4.9 vol.% with respect to the total solvent volume, which means that $CaSO_4{\cdot}0.5H_2O$ will readily precipitate, as previously demonstrated.[81]

Additionally, this approach results in a substantial increase in the saturation index (*SI*), surpassing the equilibrium *SI* for the 3 different CaSO4·nH_2O phases (i.e., anhydrite, bassanite and gypsum). This sudden increase in *SI* effectively fosters heightened nucleation rates and reduced particle sizes ensuring the formation of phase-pure bassanite nanoparticles, which is advantageous for their penetration in porous substrates (e.g., during consolidation of gypsum plasterwork). The reaction progresses under these conditions for ≈35 min.

Subsequently, the nano-bassanite particles are isolated from the reaction mixture through rotary evaporation. The resultant powder is then redispersed in 96° ethanol, sonicated for 2 min, and followed by centrifugation at 6000 rpm for 15 min. This washing procedure was performed twice to eliminate any surplus adsorbed calcein from the nanoparticle surfaces.

Note that a concentration not higher than 50 µM calcein for the synthesis of fluorescent nano-bassanite was selected because it was sufficient to yield intense luminescence during UV irradiation, while at the same time minimizing calcein usage and possible discoloration of the white precipitate due to the orange color of this additive.

High Resolution Synchrotron X-Ray Diffraction Analyses: HR-XRD analyses of fluorescent gypsum crystal samples were performed at the CRISTAL beamline of the SOLEIL Synchrotron (Paris, France), using a 2-circle diffractometer. For these measurements the selected wavelength was $\lambda = 0.67157$ Å (18 keV). The beam line is equipped with a double-crystal ^{21}Si (111) monochromator, along with nine position-sensitive Dectris Mythen II detectors, positioned on a cylinder with a radius of 720 mm, providing a 55° 2θ coverage with small gaps of 0.5° 2θ. Borosilicate glass capillaries of 0.7 mm in diameter were loaded with powder samples and rotated during data collection to improve diffracting particle statistics. The data acquisition time was 3 min per pattern, with 2 iteration per measurement to obtain a good signal-to-noise ratio over the 0° to 55° 2θ angular range. To calibrate the equipment and reduce possible shifts during experimental analysis, LaB_6 standard (NIST-SRM660, cubic, space group *Pm3m*) was used to acquire an instrumental resolution file. Under these data acquisition conditions, the angular resolution ranged from 0.02° to 0.04° (i.e., full width at half maximum, β) for the whole 2θ range.

The Rietveld refinement method was used to extract lattice parameters of gypsum, matching the experimental diffraction peaks with those calculated by Henry et al.[82] (space group *I2/c*), using FullProf Suite (v.5.10)

and the EdPCR (v.2.0) software packages. Optical quality geologic gypsum (Naica, Chihuahua, Mexico) was used as standard to compare the XRD data from the synthetized fluorescent gypsum crystals.

To investigate the microstructural variations due to organic (macro)molecule incorporation in the structure of gypsum, the Thompson-Cox-Hastings pseudo-Voigt function with axial divergence asymmetry correction was used to fit the profile of the experimental diffraction patterns. In order to reduce the statistical discrepancy between experimental and fitting values, the profiles were refined until the minimum possible values of R_{wp} and χ^2 were reached. For the experiments, the obtained R_{wp} was < 8.5, and the minimum achieved χ^2 values ranged from ≈100 to ≈130. Note that, when refining datasets of both high resolution and number of counts, it is common to obtain large χ^2 values, even though the model obtained from that data is of high quality.[83]

Microstrain fluctuations (η) and crystallite size (D_{hkl}) were calculated using the Williamson-Hall method, using six-order 0*k*0, *h*00, and 00*l* Bragg reflections obtained from the Rietveld refinement profiles, by plotting $\beta\, cos\theta$ versus 4 $sin\theta$ and adjusting the results to a linear fit as indicated below (Equation 4):

$$\beta\, cos\theta = \frac{k\,\lambda}{D} + 4\,\eta\, sin\theta \quad (4)$$

Where β is the experimental full width at half maximum peak, k is the shape factor (0.94), and λ is the synchrotron beam wavelength (0.067157 nm). For strain and crystallite size calculations, angular units were transformed into radian.

A summary containing the calculated microstrain fluctuations (η) and crystallite size (D_{0k0}, D_{h00}, and D_{00l}) is presented in Table 1 (see Results and Discussion section), where values correspond to the average η and D_{hkl}, and error is indicated as the standard deviation (σ).

Potentiometric Titration Experiments and Dissolution Resistance Tests: The effect of calcein on the nucleation and homogeneous precipitation mechanism of $CaSO_4{\cdot}nH_2O$ was studied by means of potentiometric titration using a Methrom Titrando 905, equipped with an 856 Conductivity module and an 867 pH module. Homogeneous precipitation experiments were performed at 25 °C by the continuous addition of a 0.3 M $CaCl_2{\cdot}2H_2O$ solution (0.24 mL min^{-1} addition rate) into 100 mL of a 0.1 M $(NH_4)_2SO_4$ solution in the presence of increasing concentrations of calcein (i.e., 0, 50, 150, and 250 µM). Values of Ca^{2+} potential and transmittance were continuously recorded using a Methrom Ca^{2+} selective polymer membrane electrode and a Methrom Optrode optical sensor (λ = 610 nm), respectively.

Dissolution resistance tests were performed by dispersing 40 mg of hydrated fluorescent nano-bassanite **(NB-C)**, hydrated non-fluorescent nano-bassanite **(NB)** and geologic gypsum **(GG)**, into 100 mL of milli-Q grade deionized water (pH ≈6.25, T = 25 °C). For this, samples were first sieved to a particle size range between 50 and 100 µm. Ca^{2+} potential values were continuously registered to calculate the dissolution rates using the previously described titration setup.

In order to obtain calibration curves for Ca^{2+} activity coefficients, blank experiments (i.e., in the absence of SO_4^{2-} and calcein) were performed by adding a 0.3 M $CaCl_2{\cdot}2H_2O$ solution (0.24 mL min^{-1} addition rate) into 100 mL Milli-Q grade water. Ionic strength was previously adjusted by adding NaCl (i.e., 0.25 M, calculated using PHREEQC as the equivalent ionic strength of a 0.1 M solution of $(NH_4)_2SO_4$).

In Situ Atomic Force Microscopy (AFM) Analyses: Growth experiments were carried out using a fluid cell coupled to a Bruker MultiMode 8-HR AFM powered by a Bruker NanoScope 6 AFM controller, working in contact mode at room temperature. Deflection images of the {010} surfaces of freshly cleaved gypsum crystals (from Naica, Chihuahua, Mexico) were collected using Si_3N_4 tips (SNL-10, Bruker) with nominal spring constants of 0.24 and 0.35 N m^{-1}.

For these studies, growth solutions supersaturated with respect to gypsum were prepared by mixing equimolar $CaCl_2$ and $(NH_4)_2SO_4$ solutions up to a final Ca^{2+} and SO_4^{2-} concentration of 50 mM (saturation index, SI = 0.50 with respect to gypsum, calculated using the PHREEQC software) and injected using a syringe at a flow rate of ≈0.13 mL min-1. Growth solutions included different concentrations of calcein (i.e., 0, 2.5, and 25 µM). 2D and 3D images and videos were produced using the Bruker NanoScope Analysis v1.40r1 software.

Growth directions were indexed assuming the morphological face-centered unit cell (i.e., *A*2/*a* space group) where the elongation axis corresponds with the [001] direction.

General Characterization of Solids: The obtained solids were characterized by means of standard X-ray diffraction (XRD) and Fourier Transform Infrared spectroscopy (FTIR), respectively using a Panalytical X'Pert PRO diffractometer (Cu Kα radiation, λ = 1.5405 Å, voltage 45 kV, current 40 mA, and scanning angle (°2θ) 3–70°, steps of 0.001 °2θ and goniometer speed of 0.01–2θ s^{-1}) and a JASCO FT/IR 6600 in ATR mode (4000–400 cm^{-1}, resolution of 2 cm^{-1}).

Optical microscopy photomicrographs of gypsum crystals (i.e., obtained in the presence of 0, 50, and 150 µM calcein) were acquired using a Leica DVM2000 digital microscope for size and morphology determination. Samples were irradiated with UV light (λ = 365 nm) during optical microscopy observation.

In order to determine the content of intracrystalline calcein, 20 mg of dried fluorescent gypsum and nano-bassanite samples were dissolved in hydrochloric acid (2 mL, 3 M). The resulting solutions were then analyzed using a Thermo Scientific GENESYS 50 UV-Vis spectrophotometer. Calibration curves (R^2 = 0.9999) were obtained by measuring calcein solutions with known concentrations ranging from 1 to 25 µM using the previously mentioned hydrochloric acid buffer. The amount of intracrystalline calcein (i.e., µmol calcein per mg of sample) was then calculated by the Beer-Lambert law using the maxima of absorbance at 445 nm (Figure S3 and Table S1, Supporting Information).

TEM Analyses: Micro- and nanostructural features of the synthetized nano-bassanite particles, as well as their hydration product (i.e., gypsum), were determined by means of transmission electron microscopy (TEM) using a FEI Titan S/TEM microscope (operated at 300 kV acceleration voltage). Powder samples were dispersed in absolute ethanol and sonicated for 20 s before being deposited on carbon coated Cu grids. Prepared samples were then plasma-cleaned. TEM photomicrographs were obtained using a 40 µm objective aperture. Detailed crystallographic information was obtained by measuring selected area electron diffraction (SAED) patterns, collected using a 10 µm objective aperture. A high-angle annular dark field (HAADF) detector operated in scanning TEM (STEM) mode was used to obtain Z-contrast images and compositional energy dispersive X-ray (EDX) spectra and maps.

Additional TEM analyses were performed on a FEI Titan3 Themis 300 X-FEG operating at 300 kV equipped with a FEI Super-X energy dispersive X-ray (EDX) system and a Gatan OneView CCD. For this, supersaturated $CaSO_4$ solutions (i.e., extracted at the onset of nucleation) were prepared at 25 °C by the continuous addition of a 0.3 M $CaCl_2$ solution over a 0.1 M $(NH_4)_2SO_4$ solution, in the absence and presence of 5 ppm of poly(acrylic acid). Samples were prepared by cryo-quenching as follows: a 3 µL droplet of the nucleating solution was transferred onto a plasma-treated continuous TEM grid after set times. Sample loaded grids were then rapidly plunged into liquid ethane using an FEI Vitrobot, allowing the sample to remain in its native state with any water rapidly transforming into amorphous ice.

Alternatively, in order to determine if the objects observed by full Cryo-TEM analyses were artifacts or not, grids were then transferred into a vacuum desiccator to allow the sublimation of the vitreous ice, and re-analyzed under normal TEM conditions.

Consolidation Tests: The consolidation effectiveness of ethanolic suspensions containing calcein-loaded nano-bassanite (5 g L^{-1}) was assessed using gypsum plaster as substrate. These specimens were formulated mimicking historic Islamic gypsum plaster-making at the Alhambra (Figure S10, Supporting Information). Plaster mock-ups were prepared by mixing plaster of Paris and water in a 1/1.2 ratio, in order to obtain a substantially porous substrate (≈52.5% total open porosity). The plaster paste was poured in molds and allowed to set and cure for at least 2 weeks. Cubic specimens (2×2×2 cm^3) were then obtained and further cured for at least 2 months under controlled conditions (25 °C and 90% relative humidity).

Prior to consolidation treatments, cubic gypsum plaster samples were laterally covered with parafilm. Subsequently, the calcein-loaded nano-bassanite suspension was uniformly sprayed onto one horizontal surface (upper surface) until complete imbibition was achieved (Figure 8a). This procedure was repeated up to ten times to ensure an adequate consolidation effect. Afterward, the fully treated samples were allowed to cure for one month under the *T* and RH% conditions mentioned above. Note that, at low doses, calcein does not produce drastic chromatic variations on the original color of the nano-bassanite consolidant product, while being capable to emit intense green luminescence under UV radiation (Figure S11, Supporting Information).

Penetrability of the fluorescent nano-bassanite consolidant was evaluated by irradiating vertically fractured treated gypsum plaster specimens with UV light ($\lambda = 365$ nm), while the consolidation effect was determined by means of mercury intrusion porosimetry (MIP) and drilling resistance tests (DRMS) on treated and untreated cured gypsum plaster samples.

Changes in total porosity and pore size distribution were determined using a Micromeritics Autopore III mercury intrusion porosimeter. For the MIP experiments, samples of ≈0.5 g were extracted from the top part of treated and untreated cubic plaster mock-ups. These specimens were dried in an oven at 60 °C for 8 h. Mechanical resistance of untreated and treated samples was analyzed using a SINT Technology drilling resistance measurement system. Drilling resistance tests were performed along a depth profile normal to the treated surface using the following parameters: 5 mm diameter drill-bit with a flat diamond head, 10 mm drilling depth, 20 mm min^{-1} penetration rate, and 200 rpm rotation speed. For MIP analyses 3 replicates per sample type were performed, while for DRMS at least 4 replicates per sample were performed.

Supporting Information

Supporting Information is available from the Wiley Online Library or from the author.

Acknowledgements

This research was funded by Spanish Government grant RTI2018-099565-B-I00; Spanish Government grant PID2021.125305NB.I00 funded by MCIN/AEI/10.13039/501100011033 and by ERDF "A way of making Europe"; Junta de Andalucía research group RNM-179; and University of Granada, Unidad Científica de Excelencia UCE-PP2016-05. M.B.-R. was granted with a predoctoral position funded by the Spanish Government (PRE2019-090256). This research was performed within the frame of the inter-institutional collaboration agreement "Patrimonio Cultural Árabe e Islámico (PACAI), UGR, Unidad Asociada al CSIC por la EEA-ILC (2024-2027)". HR-XRD analyses were performed at the SOLEIL Synchrotron Facility, with the invaluable technical assistance of E. Elkaim (CRISTAL Beamline, SOLEIL Synchrotron) and L. Monasterio-Guillot (Instituto Andaluz de Ciencias de la Tierra, CSIC). We are grateful for the cooperation of the Leeds Electron Microscopy and Spectroscopy Centre (LEMAS), at the University of Leeds, with the TEM measurements in both cryogenic and non-cryogenic conditions. TEM analyses were also carried out at the Centro de Instrumentación Científica (CIC), UGR. Open access was funded by the University of Granada/CBUA.

Conflict of Interest

The authors declare no conflict of interest.

Data Availability Statement

The data that support the findings of this study are available in the supplementary material of this article.

Keywords

calcium sulfate, crystal growth, heritage conservation, mineral binders, nanoparticles, nonclassical crystallization, nucleation

Received: April 1, 2024
Revised: June 11, 2024
Published online:

[1] H. Shin, S. Jo, A. G. Mikos, *Biomaterials* **2003**, *24*, 4353.
[2] P. Fratzl, *J. R. Soc., Interface* **2007**, *4*, 637.
[3] Y. Yang, X. Song, X. Li, Z. Chen, C. Zhou, Q. Zhou, Y. Chen, *Adv. Mater.* **2018**, *30*, 1706539.
[4] A. R. Parker, H. E. Townley, *Nat. Nanotechnol.* **2007**, *2*, 347.
[5] Z. Deng, Z. Jia, L. Li, *Adv. Sci.* **2022**, *9*, 2103524.
[6] U. G. Wegst, H. Bai, E. Saiz, A. P. Tomsia, R. O. Ritchie, *Nat. Mater.* **2015**, *14*, 23.
[7] E. Ruiz-Agudo, A. Burgos-Cara, C. Ruiz-Agudo, A. Ibañez-Velasco, H. Cölfen, C. Rodriguez-Navarro, *Nat. Commun.* **2017**, *8*, 768.
[8] L. Addadi, A. Berman, J. Moradian-Oldak, S. Weiner, *Croat. Chem. Acta* **1990**, *63*, 539.
[9] S. Weiner, P. M. Dove, *Rev. Mineral. Geochem.* **2003**, *54*, 1.
[10] B. Pokroy, A. N. Fitch, F. Marin, M. Kapon, N. Adir, E. Zolotoyabko, *J. Struct. Biol.* **2006**, *155*, 96.
[11] E. Weber, B. Pokroy, *CrystEngComm* **2015**, *17*, 5873.
[12] N. Nassif, N. Pinna, N. Gehrke, M. Antonietti, C. Jäger, H. Cölfen, *Proc. Natl. Acad. Sci. U.S.A.* **2005**, *102*, 12653.
[13] N. Gehrke, H. Cölfen, N. Pinna, M. Antonietti, N. Nassif, *Cryst. Growth Des.* **2005**, *5*, 1317.
[14] M. Sedlák, M. Antonietti, H. Colfen, *Macromol. Chem. Phys.* **1998**, *199*, 247.
[15] S. H. Yu, H. Cölfen, J. Hartmann, M. Antonietti, *Adv. Funct. Mater.* **2002**, *12*, 541.
[16] L. B. Mao, H. L. Gao, H. B. Yao, L. Liu, H. Cölfen, G. Liu, S. M. Chen, S. K. Li, Y. X. Yan, S. H. Yu, *Science* **2016**, *354*, 107.
[17] A. W. Xu, M. Antonietti, H. Cölfen, Y. P. Fang, *Adv. Funct. Mater.* **2006**, *16*, 903.
[18] H. Tiemann, I. Sötje, A. Becker, G. Jarms, M. Epple, *Zoologischer Anzeiger-A J. Compar. Zool.* **2006**, *245*, 13.
[19] A. Becker, I. Sötje, C. Paulmann, F. Beckmann, T. Donath, R. Boese, O. Prymak, H. Tiemann, M. Epple, *Dalton Trans.* **2005**, 1545.
[20] F. Boßelmann, M. Epple, I. Sötje, H. Tiemann, in *Handbook of Biomineralization: biological aspects and structure formation*, Vol. *1* (Eds: E. Bäuerlein, P. Behrens, M. Epple), Wiley-VCH, Weinheim, Germany **2007**, 15.
[21] S. Amini, A. Masic, L. Bertinetti, J. S. Teguh, J. S. Herrin, X. Zhu, H. Su, A. Miserez, *Nat. Commun.* **2014**, *5*, 3187.
[22] C. Rodriguez-Navarro, L. Monasterio-Guillot, M. Burgos-Ruiz, E. Ruiz-Agudo, K. Elert, *Sci. Adv.* **2023**, *9*, eadf6138.
[23] C. Rodriguez-Navarro, E. Ruiz-Agudo, A. Burgos-Cara, K. Elert, E. F. Hansen, *Langmuir* **2017**, *33*, 10936.
[24] G. Artioli, M. Secco, A. Addis, in *The Contribution of Mineralogy to Cultural Heritage*, *20* (Eds: G. Artiolli, R. Oberti), Mineralogical Society of Great Britain and Ireland, London, United Kingdom **2019**, Ch. 4.
[25] J. Ragai, *Cement Concrete Res.* **1988**, *18*, 9.
[26] M. Regourd, J. Kerisel, P. Deletie, B. Haguenauer, *Cem. Concr. Res.* **1988**, *18*, 81.
[27] P. Bel-Anzué, K. Elert, *Archaeol. Anthropological Sci.* **2021**, *13*, 177.
[28] J. Elsen, *Cement Concrete Res.* **2006**, *36*, 1416.
[29] J. Stewart, J. Moore, *Bull. Assoc. Preserv. Technol.* **1982**, *14*, 11.
[30] M. P. D. Luxán, F. Dorrego, A. Laborde, *Cem. Concr. Res.* **1995**, *25*, 1755.

[31] R. Rubio-Domene, *Yeserías de la Alhambra: historia, técnica y conservación*, Universidad de Granada, Granada, Spain **2010**.
[32] P. Bel-Anzué, A. Almagro, M. P. S. Pérez, C. Rodriguez-Navarro, *Geconservación* **2017**, *11*, 79.
[33] Charola, A. E., Koestler, R. J., in *Conservation Science: Heritage Materials* (Eds: E. May, M. Jones), The Royal Society of Chemistry, Cambridge, United Kingdom **2006**.
[34] C. M. Grossi, P. Brimblecombe, *Geol. Soc.* **2007**, *271*, 117.
[35] F. Palha, A. Pereira, J. De Brito, J. D. Silvestre, *J. Perform. Construct. Facil.* **2012**, *26*, 424.
[36] F. Jroundi, M. T. Gonzalez-Muñoz, A. Garcia-Bueno, C. Rodriguez-Navarro, *Acta Biomater.* **2014**, *10*, 3844.
[37] J. R. Molina, J. D. Suárez, E. S. Pardo, *Informes de la Construcción* **2017**, *69*, e175.
[38] S. Jiang, M. Huang, X. Wu, Z. Chen, K. Zhang, *Bull. Engin. Geol. Environ.* **2021**, *80*, 4985.
[39] X. Xu, Y. Zhou, W. Chen, Y. Gao, Q. Fu, X. Liu, C. Feng, *Minerals* **2022**, *12*, 1168.
[40] R. Rubio-Domene (Patronato De La Alhambra Y El Generalife), Sp. ES2339734A1, **2008**.
[41] B. Kahr, A. G. Shtukenberg, *CrystEngComm* **2016**, *18*, 8988.
[42] G. Magnabosco, I. Polishchuk, J. Erez, S. Fermani, B. Pokroy, G. Falini, *CrystEngComm* **2018**, *20*, 4221.
[43] A. Cotellucci, L. Pellegrino, E. Costa, M. Bruno, F. D. Pierre, D. Aquilano, E. Destefanis, L. Pastero, *Cryst. Growth Des.* **2023**, *23*, 9094.
[44] F. R. Massaro, M. Rubbo, D. Aquilano, *Cryst. Growth Des.* **2010**, *10*, 2870.
[45] M. Inoue, I. Hirasawa, *J. Cryst. Growth* **2013**, *380*, 169.
[46] Y. Y. Kim, J. D. Carloni, B. Demarchi, D. Sparks, D. G. Reid, M. E. Kunitake, C. C. Tang, M. J. Duer, C. L. Freeman, B. Pokroy, K. Penkman, J. H. Harding, L. A. Estroff, S. P. Baker, F. C. Meldrum, *Nat. Mater.* **2016**, *15*, 903.
[47] Y. Y. Kim, R. Darkins, A. Broad, A. N. Kulak, M. A. Holden, O. Nahi, S. P. Armes, C. C. Tang, R. F. Thompson, F. Marin, D. M. Duffy, F. C. Meldrum, *Nat. Commun.* **2019**, *10*, 5682.
[48] A. Lang, S. Mijowska, I. Polishchuk, S. Fermani, G. Falini, A. Katsman, F. Marin, B. Pokroy, *Chem. A Eur. J.* **2020**, *26*, 16860.
[49] K. R. Cho, Y. Y. Kim, P. Yang, W. Cai, H. Pan, A. N. Kulak, J. L. Lau, P. Kulshreshtha, S. P. Armes, F. C. Meldrum, J. J. De Yoreo, *Nat. Commun.* **2016**, *7*, 10187.
[50] Y. Y. Kim, K. Ganesan, P. Yang, A. N. Kulak, S. Borukhin, S. Pechook, L. Ribeiro, R. Kröger, S. J. Eichhorn, S. P. Armes, B. Pokroy, F. C. Meldrum, *Nat. Mater.* **2011**, *10*, 890.
[51] Y. Ning, L. Han, M. J. Derry, F. C. Meldrum, S. P. Armes, *J. Am. Chem. Soc.* **2019**, *141*, 2557.
[52] I. Izquierdo-Barba, E. Sousa, J. C. Doadrio, A. L. Doadrio, J. P. Pariente, A. Martínez, F. Babonneau, M. Vallet-Regí, *J. Sol-Gel Sci. Technol.* **2009**, *50*, 421.
[53] D. Gebauer, A. Volkel, H. Cölfen, *Science* **2008**, *322*, 1819.
[54] E. M. Pouget, P. H. Bomans, J. A. Goos, P. M. Frederik, G. de With, N. A. Sommerdijk, *Science* **2009**, *323*, 1455.
[55] W. J. E. M. Habraken, J. Tao, L. J. Brylka, H. Friedrich, L. Bertinetti, A. S. Schenk, A. Verch, V. Dmitrovic, P. H. H. Bomans, P. M. Frederik, J. Laven, P. van der Schoot, B. Aichmayer, G. de With, J. J. De Yoreo, N. A. Sommerdijk, *Nat. Commun.* **2013**, *4*, 1507.
[56] C. Rodriguez-Navarro, A. Burgos-Cara, F. D. Lorenzo, E. Ruiz-Agudo, K. Elert, *Cryst. Growth Des.* **2020**, *20*, 4418.
[57] D. Gebauer, H. Cölfen, A. Verch, M. Antonietti, *Adv. Mater.* **2009**, *21*, 435.
[58] D. Gebauer, J. D. Gale, H. Cölfen, *Small* **2022**, *18*, 2107735.
[59] M. A. Bewernitz, D. Gebauer, J. Long, H. Cölfen, L. B. Gower, *Faraday Discuss.* **2012**, *159*, 291.
[60] A. Picker, M. Kellermeier, J. Seto, D. Gebauer, H. Cölfen, *Zeitschrift für Kristallographie-Crystalline Mater.* **2012**, *227*, 744.
[61] A. Rao, J. K. Berg, M. Kellermeier, D. Gebauer, *Eur. J. Mineral.* **2014**, *26*, 537.
[62] S. E. Wolf, J. Leiterer, V. Pipich, R. Barrea, F. Emmerling, W. Tremel, *J. Am. Chem. Soc.* **2011**, *133*, 12642.
[63] L. Nicoleau, A. E. Van Driessche, M. Kellermeier, *Cem. Concr. Res.* **2019**, *124*, 105837.
[64] P. Duchstein, P. I. Schodder, S. Leupold, T. Q. Dao, S. Kababya, M. R. Cicconi, D. de Ligny, V. Pipich, D. Eike, A. Schmidt, D. Zahn, S. E. Wolf, *Angew. Chem., Int. Ed.* **2022**, *61*, e202208475.
[65] J. T. Avaro, S. L. Wolf, K. Hauser, D. Gebauer, *Angew. Chem., Int. Ed.* **2020**, *59*, 6155.
[66] M. Burgos-Ruiz, G. Pelayo-Punzano, E. Ruiz-Agudo, K. Elert, C. Rodriguez-Navarro, *Chem. Commun.* **2021**, *57*, 7304.
[67] C. Jia, L. Wu, J. L. Fulton, X. Liang, J. J. De Yoreo, B. Guan, *J. Phys. Chem. C* **2021**, *125*, 3415.
[68] (a) M. Ilett, H. M. Freeman, Z. Aslam, J. M. Galloway, D. P. Klebl, S. P. Muench, I. J. McPherson, O. Cespedes, Y. Y. Kim, F. C. Meldrum, S. R. Yeandel, C. L. Freeman, J. H. Harding, R. M. D. Brydson, *J.Micr.* **2022**, *288*, 155. (b) M. Ilett, M. Afzali, B. Abdulkarim, Z. Aslam, S. Foster, M. Burgos-Ruiz, Y. Y. Kim, F. C. Meldrum, R. M. D. Brydson, *J. Micr.* **2024**, https://doi.org/10.1111/jmi.13300.
[69] S. Sun, L. B. Mao, Z. Lei, S. H. Yu, H. Cölfen, *Angew. Chem., Int. Ed.* **2016**, *55*, 11765.
[70] Y. Xu, K. C. Tijssen, P. H. Bomans, A. Akiva, H. Friedrich, A. P. Kentgens, N. A. Sommerdijk, *Nat. Commun.* **2018**, *9*, 2582.
[71] M. Y. Lin, H. Lindsay, D. A. Weitz, R. C. Ball, R. Klein, P. Meakin, *Nature* **1989**, *339*, 360.
[72] Y. W. Wang, F. C. Meldrum, *J. Mater. Chem.* **2012**, *22*, 22055.
[73] A. Saha, J. Lee, S. M. Pancera, M. F. Bräeu, A. Kempter, A. Tripathi, A. Bose, *Langmuir* **2012**, *28*, 11182.
[74] F. Jones, *CrystEngComm* **2012**, *14*, 8374.
[75] Y. Zhang, D. Xue, *J. Mol. Struct.* **2020**, *1210*, 128043.
[76] C. V. Putnis, E. Ruiz-Agudo, *Elements* **2013**, *9*, 177.
[77] E. Doehne, C. A. Price, *Stone Conservation: An Overview of Current Research*, 2nd ed., Getty Conservation Institute, Los Angeles, USA **2011**.
[78] M. Burgos-Ruiz, K. Elert, E. Ruiz-Agudo, H. Cölfen, C. Rodriguez-Navarro, *Small* **2023**, *19*, 2300596.
[79] M. L. Bella, R. Besselink, J. P. Wright, A. E. Van Driessche, A. Fernandez-Martinez, C. Giacobbe, *J. Appl. Crystallogr.* **2023**, *56*, 660.
[80] S. Reigl, A. E. Van Driessche, E. Wagner, G. Montes-Hernandez, J. Mehringer, S. Koltzenburg, W. Kunz, M. Kellermeier, *ACS Sustainable Chem. Eng.* **2023**, *11*, 8450.
[81] U. Tritschler, M. Kellermeier, C. Debus, A. Kempter, H. Cölfen, *CrystEngComm* **2015**, *17*, 3772.
[82] P. F. Henry, M. T. Weller, C. C. Wilson, *J. Appl. Crystallogr.* **2009**, *42*, 1176.
[83] B. H. Toby, *Powder Diffr.* **2006**, *21*, 67.